PASJ: Publ. Astron. Soc. Japan **47**, 105–114 (1995)

The X-Ray Telescope on board ASCA

Peter J. SERLEMITSOS, Lalit JALOTA, and Yang SOONG
NASA, Goddard Space Flight Center(code 666), Greenbelt, MD 20771, USA

Hideyo KUNIEDA, Yuzuru TAWARA, Yoshiyuki TSUSAKA, Hisanori SUZUKI, Yasuhiro SAKIMA, Takashi YAMAZAKI, Hidenori YOSHIOKA, Akihiro FURUZAWA, and Koujun YAMASHITA
Department of Astrophysics, Nagoya University, Furo-cho, Chikusa, Nagoya 464

Hisamitsu AWAKI
Department of Physics, Kyoto University, Sakyo-ku, Kyoto 606-01
and
Masayuki ITOH, Yasushi OGASAKA, Hirohiko HONDA, and Yasuhiro UCHIBORI
Institute of Space and Astronautical Science, Yoshinodai, Sagamihara, Kanagawa 229

(Received 1994 June 10; accepted 1994 November 25)

Abstract

The ASCA instrument uses identical conical foil X-ray mirrors for its four telescopes. One of the major advantages of ASCA's telescopes is the first time ever use of X-ray imaging over a broad energy band and high throughput for conducting astronomical spectroscopy. Nested thin foil reflectors make possible a large effective area up to 10 keV, even under the tight weight restriction of the ASCA spacecraft. The expected characteristics of the ASCA mirrors are summarized based on ray tracings and pre-flight calibrations. The total effective area of four telescopes at 1 and 7 keV are $\sim$ 1200 and 600 cm^2, respectively. The image size (half power diameter : HPD) is about 3′. The field of view is 24′ and 16′ FWHM for 1 and 7 keV, respectively. Observations of several X-ray sources from space during the performance verification phase have confirmed those performances as well as the alignment of the optical systems.

Key words: Instruments: detectors — Telescopes — X-rays: general

1. Introduction

Imaging in the X-ray band has been implemented before ASCA on three major astronomical instruments, namely Einstein (Van Speybroeck 1979), EXOSAT(de Korte et al. 1981), and ROSAT(Aschenbach 1988) observatories. In each case, however, observations were limited by the mirror to a relatively narrow, low energy band. Thus, although we have known for more than a decade that emission and absorption spectral features around 7 keV due to K-band transitions in iron, the most abundant heavy element in nature after oxygen, appear prominently in the spectra of many X-ray sources, such features could not be studied with the previous imaging instruments because they must be observed at energies well above their upper level cutoff.

In order to extend the mirror efficiency to energies high enough to adequately cover the iron K-band, it is necessary to design mirrors where photons are reflected at smaller incident (grazing) angles than were for previous instruments. Consequently, it requires a large number of confocal reflectors, seen almost edge-on, to fill the aperture and build up the effective area typically needed for most astronomical observations. A most straight forward way for nesting reflectors confocally is to place them in a cylindrically symmetric arrangement (Serlemitsos 1981). Since reflector edges cause obscuration essentially independent of the angle of incidence, they fill in more and more of the available mirror aperture as the grazing angle of incident photons is reduced. Therefore, a drastically thinner reflector substrate is essential if we are to maintain a high mirror throughput.

BBXRT, a US Space Shuttle mission flown in 1990 December, was the first X-ray astronomy experiment to pioneer telescopes effective over a broad energy band at moderate spatial resolution (Serlemitsos 1988). Its nested thin foil mirrors were constructed from thin aluminum foil reflectors made of high luster commercial aluminum. Foil segments were first formed into conical reflectors which were then coated with acrylic lacquer for increased smoothness, followed by $\sim$ 500 Å of vacuum deposited gold for enhanced reflectivity in the X-ray band. Two BBXRT telescopes (40 cm in diameter, 3.77 m of focal length) had effective area of 450 cm^2 and 180 cm^2 at 1 keV and 7 keV, respectively. The mirror weight of two telescopes was 40 kg.

ASCA (Advanced Satellite for Cosmology and Astro-

Table 1. XRT design parameters.

Mirror substrate	127 μm aluminum foil
Mirror surface	Acrylic lacquer 10 μm + Au (500 Å)
Mirror length	100 mm
Mirror number	120 foils
Outer (inner) diameter	345 (120) mm
Focal length	3500 mm
Incident angle	0.°24–0.°70
Number of telescopes	4
Mirror weight	9882 g(M0), 9855 g(M1), 9795 g(M2), 9808 g(M3)
Total mirror weight	39340 g
Geometrical area	558 cm^2/telescope
Field of view	24′ (@1 keV), 16′ (@7 keV)

physics, launched on 1993 February 20; Tanaka et al. 1994), known before launch as ASTRO-D is the fourth Japanese X-ray astronomy mission and was developed in collaboration between the USA and Japan. The four ASCA mirrors were an improved version of the BBXRT design with particular emphasis on high energy efficiency and ultra light weight. The combined effective area exceeds 1200 cm^2 and 600 cm^2 at 1.5 and 7 keV, respectively. The total weight (including thermal shields) of four mirrors was less than 40 kg. Two types of focal plane detectors were used: the Gas Imaging Spectrometer (GIS: Ohashi et al. 1991; Kohmura et al. 1993) and the Solid-state Imaging Spectrometer (SIS: Burke et al. 1991).

In this paper we intend not only to give general introduction of the X-ray Telescope (XRT) but also to provide the ASCA investigators with adequate information on the XRT design and performance to facilitate the interpretation of the data. In section 2, we summarize the XRT design parameters and describe the strategy for evaluating its performance through a combination of ray tracing and pre-flight calibrations (described in more detail by Tsusaka et al. 1993). Section 3 describes the expected performance of the ASCA telescopes based on the above strategy. In section 4, we compare predictions with selected flight data obtained during the Performance Verification (PV) phase, that is roughly the first seven months of the mission.

2. XRT Instrumentation

2.1. Reflectors

As explained earlier, efficient reflection of X-rays occurs at small grazing angles. Given a reflection surface material, for each photon energy there is a critical reflection angle beyond which X-ray reflectivity decreases rapidly. Thus for the gold XRT surface the critical angle at 7 keV is 0.°6. When X-rays impinge on a surface at such an angle, the effective surface width is reduced by a factor of 100 so that the surface is seen almost edge-on. To avoid excessive edge obscuration, we must therefore use a very thin substrate. We chose for ASCA XRT a 0.127 mm aluminum foil. It is not realistic to shape a thin foil into aspherical surfaces as used in the Wolter Type I geometry. Hence the approximate conical geometry of XRT. It is important to note, however, that this conical approximation has not been the dominant source thus far in limiting the image size (blur) achieved with foil mirrors, which is roughly six fold larger than what this approximate geometry allows. As the BBXRT, the XRT reflectors are fixed with conical segments which span approximately 90°. Their $\sim$ 100 mm length was chosen principally for ease of handling.

Most technical details of reflector preparation have been published elsewhere (Serlemitsos 1988). For XRT reflectors we used an alternative approach for curving the foil into the desired conical shapes, as contrasted with the mechanical rolling used previously. This involved constraining the foil against conical mandrels then stress relieving it at 140°C. Because of the limited number of mandrels, matching to actual curvature was only approximate requiring small shape adjustments during assembly. Although the foil used was of the highest available quality, additional surface smoothing is essential for efficient X-ray reflection. Since mechanical polishing is out of the question for such a thin foil, reflectors were dipped in a lacquer imparting on them a $\sim$ 10 μm acrylic layer which effectively smoothes over surface defects on a scale of 100 μm or smaller and up to several micron deep. Because of the strong dependence of the reflection efficiency on the atomic number Z of the surface, 500 Å of gold was vacuum deposited over the acrylic layer. The final surface roughness was measured to be near 3 Å r.m.s. height for the surface wave length range from 5 to 100 μm. The back side of the reflectors is of course just as smooth but

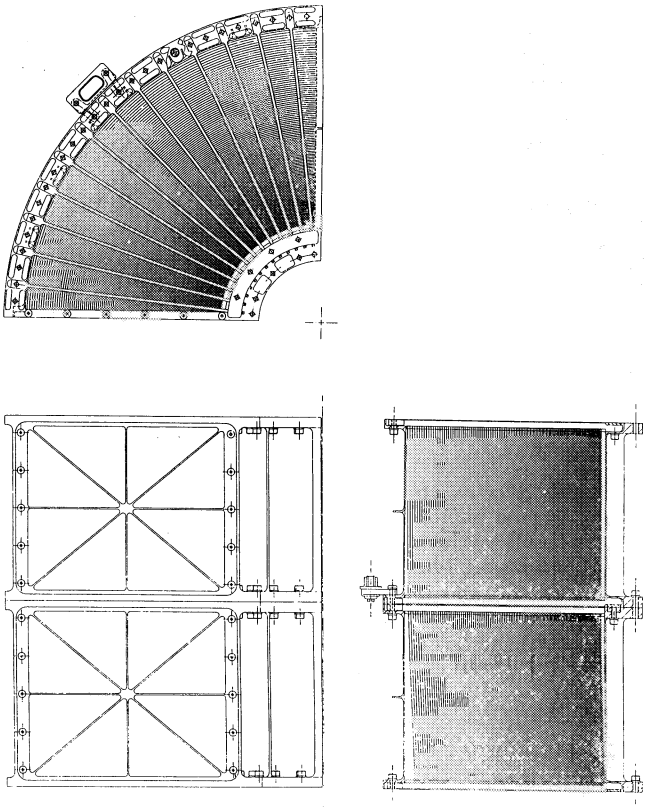

Fig. 1. XRT quadrant housing. 120 foil reflectors are installed in each of the two layers. Also shown are the 13 slotted radial bars which support the reflectors in the housing.

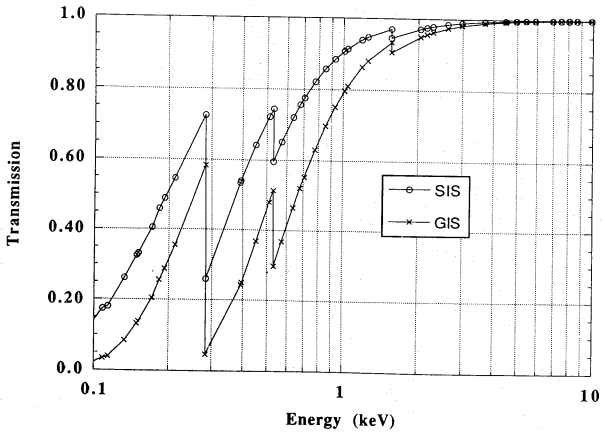

Fig. 2. Transmission of the thermal shield. aluminized Polyethylene Terephthalate (PET) film is supported by a stainless steel mesh whose transmission is 94.2%. Film thickness is 0.22 μm and 0.54 μm for the SIS and GIS respectively. The figure shows three absorption edges for each graph, at 0.28, 0.53, and 1.5 keV, due respectively to carbon and oxygen in the PET and to the aluminum reflecting coating.

with a much lower Z. As we will see later, this has resulted an additional low energy "stray light" component over what is normally attributed to single reflections of X-rays incident from outside the field of view.

2.2. *Telescope Design*

The XRT aperture is an annulus with inner and outer diameters of 120 and 345 mm respectively. Filling this aperture are 120 reflectors stacked as tightly as possible without causing interference among neighbors for axial rays. Interference or shadowing (vignetting) does occur for off-axis rays which accounts for the reduction in effective area for such rays. Mirror assembly is in quadrants. In each quadrant housing, reflectors are supported at their top and bottom edges by 13 slotted radial supports which also serve for reflector shape adjustments and group alignment. Imaging at grazing incidence requires an even number of reflections so each complete XRT (two reflections) is made up of eight such quadrants arranged in two layers with a small gap between them. There is a one-to-one correspondence among reflectors in the two layers with each cone angle at the lower layer being three times larger than the cone angle of the corresponding top reflector. The requirement that all cones in each layer are confocal (i.e. have the same apex) translates in a linear relationship between cone angles and the corresponding reflector radii. XRT design parameters are summarized in table 1. The outer mirror diameter was limited by the satellite mounting plate which had to accommodate four mirrors. The 3500 mm focal length was attained following launch through a 1200 mm extension of the optical bench. The plate scale is 1 mm arcmin^{-1}.

2.3. *Thermal Shield*

If allowed to radiate to cold space, the thermally isolated XRT would become much colder than any other part of the instrument. This would create two major problems. An unobstructed XRT would be the conduit to space of most volatile material from the rest of the spacecraft. Many of these would condense on a cold XRT contaminating its reflecting surfaces and severely affecting performance. The second problem is that there is going to be a top-to-bottom XRT thermal gradient likely to cause distortions that would also degrade imaging performance. To prevent such a situation, two actions were taken. 1) Heaters were installed on the mirror housing; 2) a very thin thermal shield was placed over the entire aperture of each mirror. The principal component of the shield is aluminized Polyethylene Terephthalate(PET) film, specially developed by the TORAY Co. to thicknesses of 0.22 and 0.54 μm for the SIS and GIS detectors respectively. The 300 Å aluminum outer coating has the low thermal emissivity needed to reduce radi-

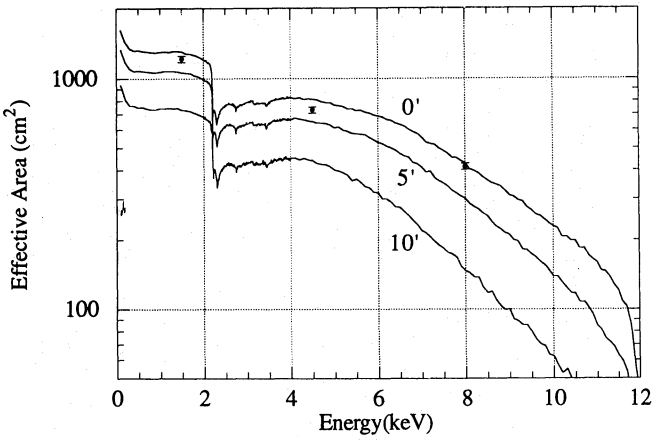

Fig. 3. Effective area: energy dependence at the three off-axis angles as indicated. The total effective area of four telescopes is plotted against photon energy. Solid circles are the on-axis area measured at the beam line facility, and the lines are calculated by the ray tracing program. The sharp drop at about 2.2 keV is attributed to the gold M-edge complex.

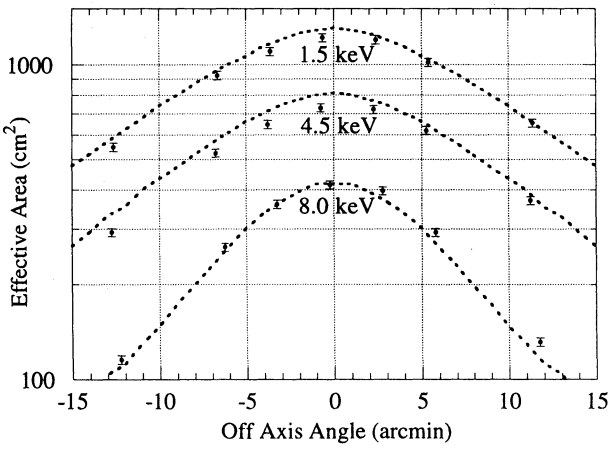

Fig. 4. Effective area: angular response at the three indicated photon energies. The effective area drops for off-axis incidence because of reflector-to-reflector shadowing (vignetting). Note that the FWHM is 22′, 20′, and 16′ at the three energies. The isolated points in each graph are data points measured at the ISAS beam line.

ation and guards the film as well from atomic oxygen bombarding which is known to severely degrade exposed PET film at the ASCA altitude of 500 km.

To survive in the severe acoustic and vibration environment during launch, the film is supported by a 0.15 mm thick stainless steel mesh whose 3 mm pitch gives it a geometric transmission of 93%. The overall thermal shield transmission is shown in figure 2. At the O-Kα(523 eV) the total transmission is about 70 and 50% for the two thicknesses used.

3. Expected Performance

The ASCA data analysis invariably requires knowledge of the XRT performance at a level of detail that would be very difficult to obtain from calibrations alone. For that reason, the strategy all along has been to use ray tracing as a tool that can bridge gaps between isolated pre-flight and flight calibrations, effectively allowing us to characterize the XRT performance at any combination of photon energy and incident angle. Aside from geometry, ray tracing involves several parameters, including the optical constants for the surface, whose values must be established or confirmed before its intended use is deemed reliable. Much of the detail on the ray tracing program and the tuning of its parameters is given in Tsusaka et al. (1993, 1995). Pre-flight calibrations were carried out at several facilities including the 30 m beam at the Institute of Space and Astronautical Science (ISAS; cf. Kunieda et al. 1993), a 300 m beam at White Sands (N.M., USA) and the synchrotron radiation facility (UVSOR) of the Institute of Molecular Science (Okazaki, Japan). In the following sections we compare ray tracing predictions with pre-flight data.

3.1. Effective Area: Energy Dependence

Reflection efficiencies for a gold surface are most reliably known below 2 keV (Henke et al. 1982). Difficulties arise at the gold M absorption edges near 2.2 keV and at the higher energies where existing data sets differ. Our approach called for absolute reflectivity measurements at three characteristic K line energies, Al (1.49), Ti (4.5), and Cu (8.0 keV). Additionally, we used monochromatic X-rays from the synchrotron facility to scan the region 2–4 keV. Combining all these data, we derived a semi-empirical relation for the optical constants for use in the ray tracing program.

X-rays from a point source are imaged at the focal plane in a complex distribution which is both sharply peaked (specular reflection) but also extends to many arcminutes from the centroid due to scattering. Such scattering is both energy dependent when caused by surface roughness (Kunieda et al. 1986) as well as energy independent when caused by figure error and mis-alignment of the many foils. XRT blurring is characterized by both these types of scattering. In data analysis, one integrates from the image centroid out a radius which invariably results in only partial accounting of the imaged photons. Consequently, ray tracing must faithfully reproduce the distribution of the image blur as a function of photon energy.

In figure 3 we show the total effective area of four telescopes vs. photon energy thus obtained by integrating

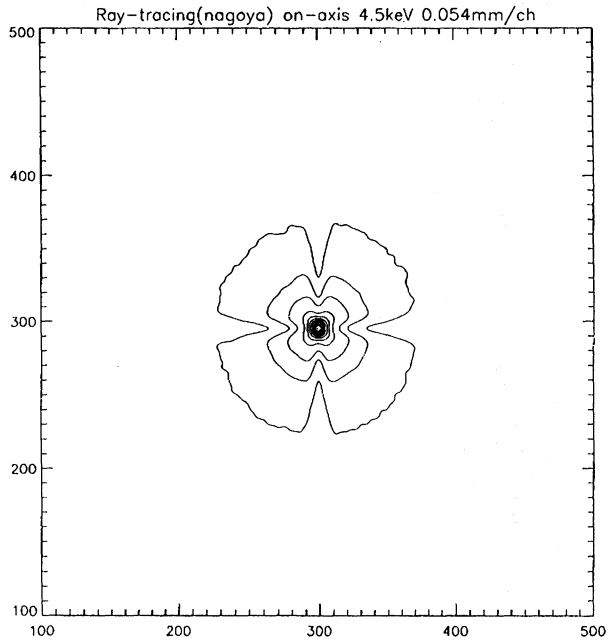

Fig. 5a. Simulated on-axis XRT image for 4.5 keV X-rays. The shadows are caused by blocked off quadrant boundaries. The frame size is $\sim$ 22′ square, that is the SIS detector size. The contour levels are every one tenth of the peak flux.

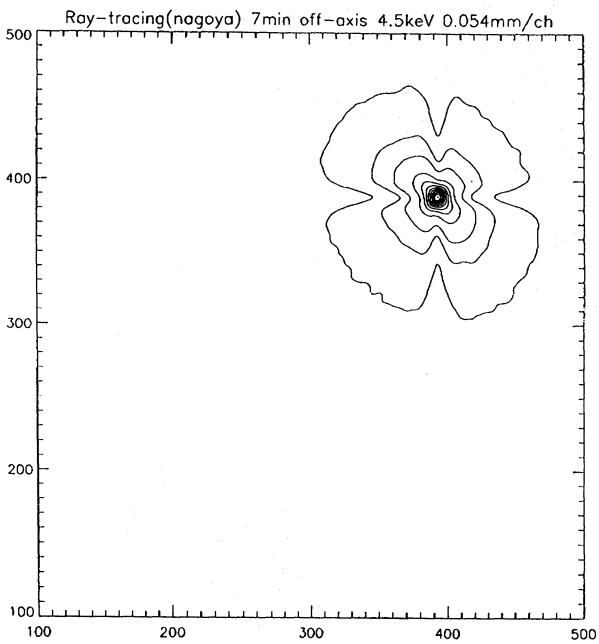

Fig. 5b. Simulated seven arcmin off-axis XRT image for 4.5 keV X-rays. Image shrinking in the radial direction is caused by vignetting. A small elongation is also seen in the tangential direction

inside a 12′ diameter circle, and for three off-axis angles (0′, 5′, and 10′). As seen, the on-axis effective area is 1200 and 420 cm^2 at 1 and 8 keV respectively. The energy dependence shown in the figure is essentially due to the reflectivity of gold. The sudden drop in efficiency at the gold M edges is readily seen.

3.2. *Angular Response*

For on-axis incidence, the only geometric obscuration is due entirely to reflector edges and supports. As mentioned above, off-axis rays suffer additional obscuration caused by shadowing (vignetting) among reflectors. This component becomes progressively larger with increasing off-axis angle. The vignetting introduces an energy dependence in the XRT angular response because imaging at high energies is most efficient at the innermost reflectors with the smaller cone angles, tighter packing and thus higher susceptibility to shadowing. The XRT angular response as derived from ray tracing is shown in figure 4. Note that the full width at half maximum (FWHM) of the response is 24′ and 16′ for 1.5 and 8.0 keV respectively. The data also shown in the figure were obtained from measurements at the ISAS beam line. Note that the data give a little flatter response, possibly because of reflector misalignments. It could also cause the data points in figure 3 lower than the expected value at some energies.

3.3. *Image Quality*

In figure 5a we show a ray traced image of an on-axis source at 4.5 keV. The four radial shadows are due to the quadrant boundaries where we have blocked the XRT aperture because of the poorer reflector performance near their free ends of each quadrant. In describing the profile of the image, we most often refer to two functions: The encircled energy function (EEF) which gives the flux within a circle of given diameter or radius and its differential form, the point spread function (PSF), which gives the flux density at every location.

The sharp peak (1/r dependence) near the image centroid is typical of grazing incidence optics. In the case of XRT, we find about 10% of the flux contained within a 30″ diameter circle. Fluctuation of the surface normal vector on various scales results in broadening of the image over what would be consistent with a precise conical geometry and flawless surfaces. Most dominant is the mm scale waviness, often referred to as "orange peel" or "medium scale figure error". This broadening has no energy dependence and is typically characterized by an EEF where the half power diameter (HPD) is three arcmin. The radial dependence of the EEF is shown in figure 6a whereas the PSF is shown in figure 6b. As mentioned earlier, XRT is also characterized by a small

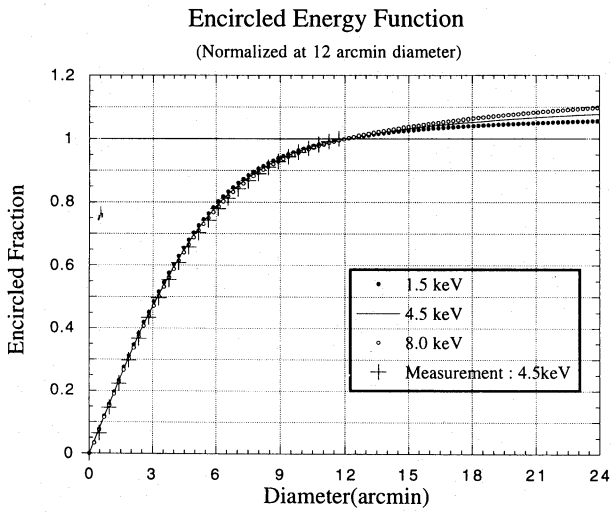

Fig. 6a. Simulated encircled energy function (EEF) at Al-K, Ti-K, and Cu-K energies. The function is normalized to 1.0 at 12′ diameter in all three cases. Note that there is little difference at the three energies inside this circle. Also shown with crosses are measured data points for the Ti-K X-rays.

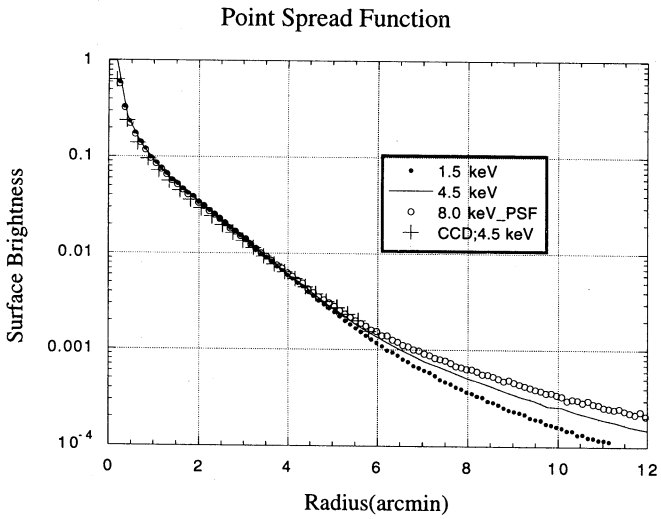

Fig. 6b. Simulated point spread function for the same three energies as in figure 6a shown as a function of radius from the image center. Again, measured data points for Ti-K X-rays are also shown with crosses.

amount of energy dependent broadening, resulting from smaller scale surface roughness, which is predominantly seen in the wings of the image distribution. Outside 12′ diameter, such scattering ranges from 8% for Al-K to 17% for Cu-K and is consistent with what is expected from the 3 Å surface roughness measured for the XRT surfaces using an X-ray pencil beam.

3.4. Off-Axis Images

From figure 5a we see that, with the exception of the four shadows, the on-axis XRT image is axially symmetric. In figure 5b on the other hand we show the XRT image for a 7′ off-axis source. Note that, in addition to the shadows, the image is also flattened or clipped in the off-axis direction. The missing portions are caused by the previously described vignetting effects. Since vignetting is more severe at high energies, off-axis images have distinct energy dependent profiles, i.e. they are "softer" in the off-axis direction and "harder" in a direction tangential to this.

3.5. Stray Light

The XRT geometry does not allow photons reaching the focal plane without being intercepted by either a top (primary) or a bottom (secondary) reflector. However, it is possible for singly reflected rays to get through the mirror. Any photons reaching the focal plane without undergoing the nominal sequence of two successive reflections from the front (gold) surfaces of the two XRT layers constitute stray light, in that they are not properly imaged but form instead a quasi diffuse background. This includes the situations where one of two reflections involved the back of a reflector where the smooth acrylic surface has considerable reflectivity below about 2 keV. Figure 7 shows the simulated stray light pattern due to a source one degree off axis. The normal two-reflection image is not shown since it is off the field of view. Instead we see the singly reflected component at the top and right areas of the figure as well as the component involving the reflector back side at the left and bottom areas. The dark lanes in the figure are the shadows of radial reflector supports. Stray light has the greatest impact whenever we are observing a weak source near a source intense enough to so contaminate the field of view. It also affects studies of the cosmic X-ray background (CXB) since a small fraction of the out of view component, in the annulus roughly 0.°5–2°, mixes in at the detector with the direct component. Though stray light is at a level almost four orders of magnitude below the original intensity, its effect is non negligible after integration over the applicable solid angle.

4. Examples of Flight Data

Flight calibration data are important because they provide the most recent information on instrument performance and the only available information following the stressful launch conditions. On the other hand, we are dealing with astronomical sources, many with varying intensities, whose spectral parameters are not

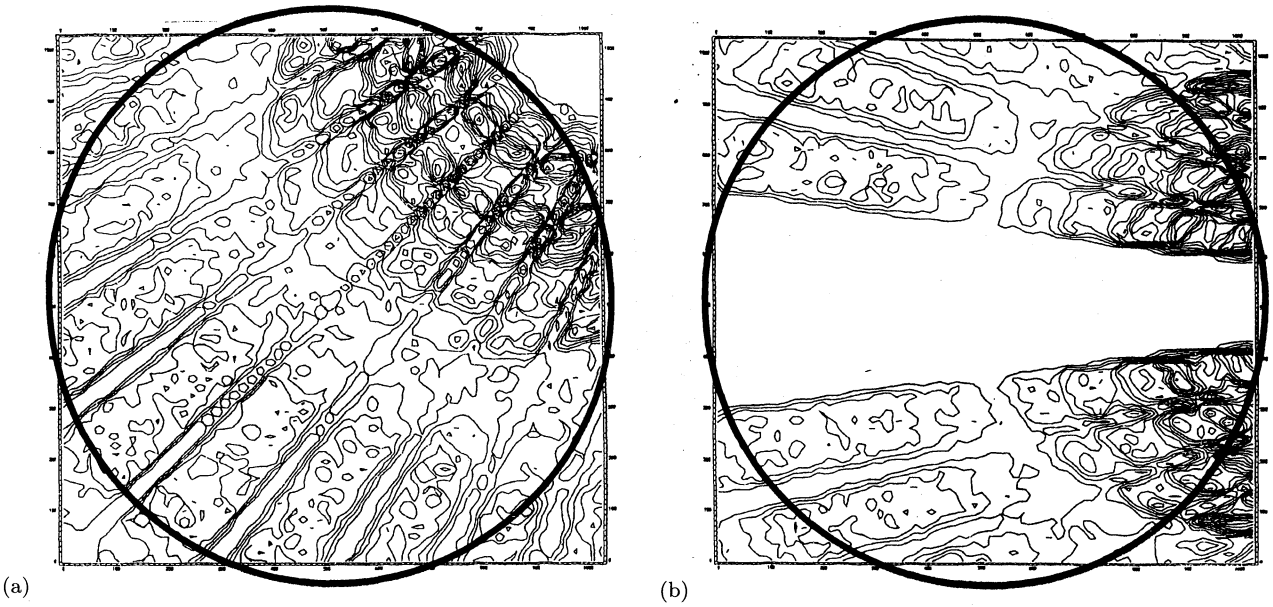

Fig. 7. Simulated stray light beam patterns from a source one degree off-axis. a) toward the upper right corner of the figure; b) to the right of the figure. In both cases, the primary source images are off the field of view. Circles indicate the GIS field of view(52′ in diameter). The contour levels are every one twentieth of the maximum flux.

precisely known. We always of course use calibration sources with simple spectra that have been well studied before with a variety of instruments and whose spectral parameters are, therefore, well constrained (i.e. the Crab nebula). ASCA flight calibrations were carried out from 1993 April through October, a period known as the Performance Verification (PV) phase.

4.1. The Crab GIS Spectrum

The well known supernova remnant Crab nebula is as ideal a calibration source as one can find in space because it has a steady flux and a simple power law spectrum with photon index of about 2.09 and neutral hydrogen column density in the line of sight of about 3×10^{21} cm^{-2} (Turner et al. 1989). On the other hand, it does have energy dependent extent which limits its usefulness for imaging instruments. The Crab nebula was observed several times in 1993 April and again in September, at more than 10 off-axis positions. After the determination of the XRT optical axis and response matrix at each position, the spectra with both GIS detectors are well fitted using parameters consistent with the previous information (small corrections for the optical constants of the mirror in high energies as are explained by Tsusaka et al. 1993). With a representative GIS spectrum shown in figure 8 (off axis angle of 4′), $N_{\rm H} = (2.6 \pm 0.6) \times 10^{21}$ cm^{-2} and $\Gamma = 2.084 \pm 0.014$ are obtained with the chi square of 210 for the degree of freedom of 230.

Below the gold M edge, we need some more considerations, because the flight data around 2 keV seems to be enhanced more than we expected based on the optical constants we confirmed. Since any structure has never been reported from Crab, we are carefully looking at the telescope and detector response.

Crab is too bright for the SIS detectors, for which we must therefore use fainter and not as well known sources, such as the quasar 3C 273.

4.2. Image Profile of SN 1993J and 3C 273

In spite of the fact that ASCA has only moderate imaging capability, ray tracing indicates that the cusp-like XRT image profile makes it possible to partially separate sources as close as 30″. The recent supernova remnant 1993J (Kohmura et al. 1994) is an important example of that capability. The source was observed at the beginning of the PV phase, before the XRT characteristics had been calibrated. The supernova appeared only three arcmin from the bright nucleus of M81 and less than one arcmin from another known source in the same galaxy. Figure 9 shows the composite of the three sources. SN 1993J is the second brightest source in the surface map, clearly distinguishable from the adjacent fainter source.

In figure 10 we show an example of the encircled energy functions for a point source, 3C 273, observed with the two SIS detectors. To avoid compromising the measurement with aspect uncertainties, we used only data when the attitude determination was inferred directly from the

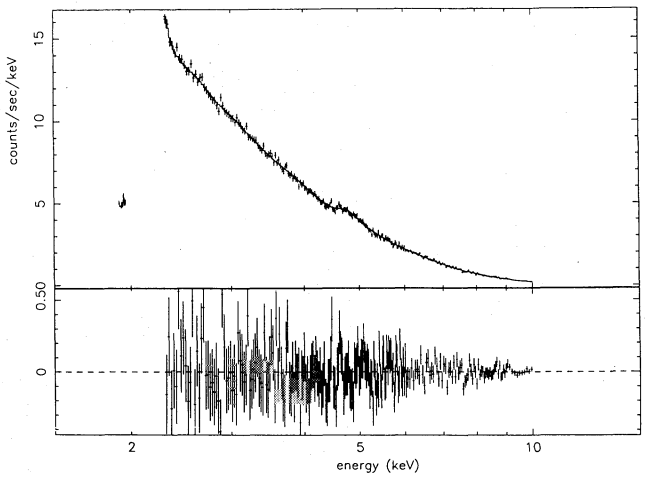

Fig. 8. The observed Crab spectrum with GIS 2 accumulated within 12′ diameter and fit above 2.3 keV with a power law and absorption. The off axis angle of Crab is $\sim$ 4′ from the optical axis. The structure seen around 4.5 keV is due to the GIS response. The best fit parameters are a photon index of 2.084 ± 0.014 and $N_{\rm H}$ of $(2.6 \pm 0.6) \times 10^{21}$ cm^{-2} (chi square of 210 with d. o. f. of 230). The lower panel shows the residual of the data from the model.

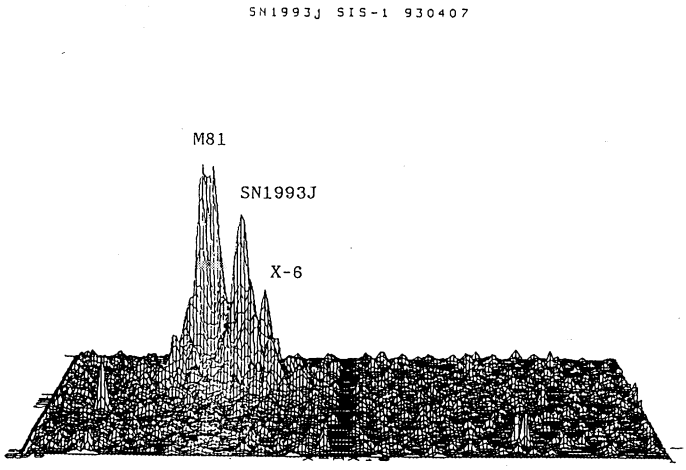

Fig. 9. SIS surface map of M81, a site of a supernova (SN 1993J) explosion soon after the start of the ASCA performance verification phase. SN 1993J appears as the second brightest source. The angular separation between the supernova and the previously known source X-6 is less than 1′.

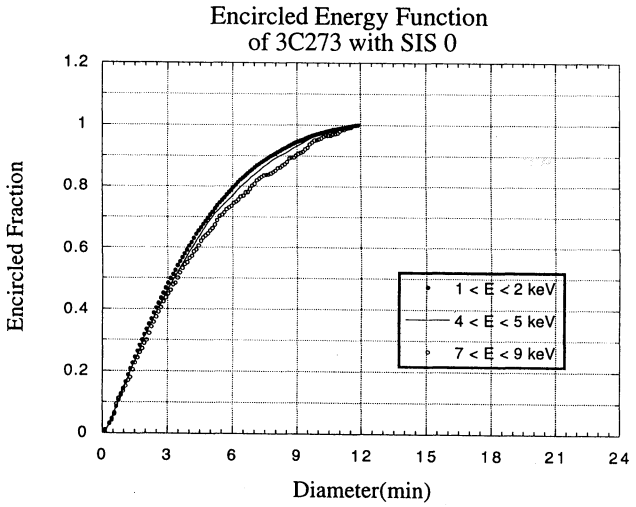

Fig. 10. The XRT encircled energy function from data obtained during the observation of the bright quasar 3C 273. Three energy bands are selected as (1.0–2.0 keV), (4.0–5.0 keV), (7–9 keV), so that one can compare them with the simulated results at 1.5, 4.5, and 8 keV in figure 6a.

star sensor. The EEFs for energies up to about several keV are almost identical but we do see some broadening above that energy. The encircled energy in the flight data (figure 10) seems to be less than pre-launch data in figure 6a. Though quantitative evaluation of broadening is under investigation, we suspect some increase of scattering in orbit. With the GISs, the sharp XRT core is somewhat smeared due to a position determination error of about 0.5 mm (Ohashi et al. 1995). This degradation is confined to the sharp core, as evidenced by an almost identical 3′ EEF half power diameter as measured with the SIS. In point source analyses, it is recommended that investigators use a 6′ diameter for accumulating source counts.

4.3. Stray Light Pattern

To verify the previously simulated stray light patterns shown in figure 7, we observed the two intense sources, the Crab nebula and Sco X-1, at the corresponding ray traced positions of figure 7. Thus, both sources were observed one degree off-axis, with the Crab at an azimuth angle of 45° relative to quadrant boundaries, whereas Sco X-1 at 0° azimuth, i.e. along such a boundary. Figure 11a is the observed focal plane distribution due to stray light from the Crab while figure 11b is similarly the stray light from Sco X-1. The patterns are strikingly similar to those of figure 7. We note with interest the broad and well defined shadow when a source, even as intense as Sco X-1, is observed along a quadrant bound ary. This effect can be used to advantage whenever we want to study a weak target in the vicinity of a much stronger source.

The quantitative evaluation of stray light is done by comparing the observed patterns in figure 11 with the simulated ones in figure 7. An X-ray source placed 1 degree off gives on the order of 0.01% of its flux into a circle of 3′ diameter at the detector center. Similarly, stray light from the CXB outside the field of view is calculated

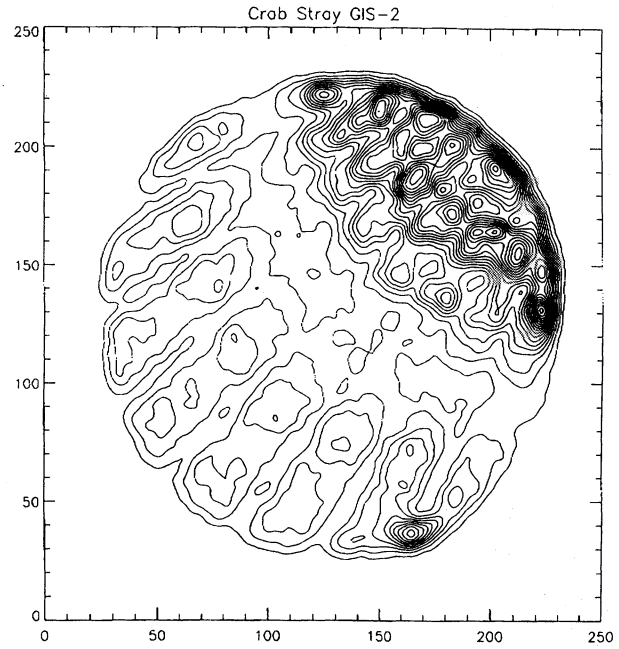

Fig. 11a. One degree off-axis observation of the Crab nebula at 45° azimuth (i.e. source at upper right of the figure). The round shape is the GIS field of view of 52′ in diameter. These data allow a direct comparison with the ray traced simulation shown in figure 7a. The contour levels are every one twentieth of the peak flux.

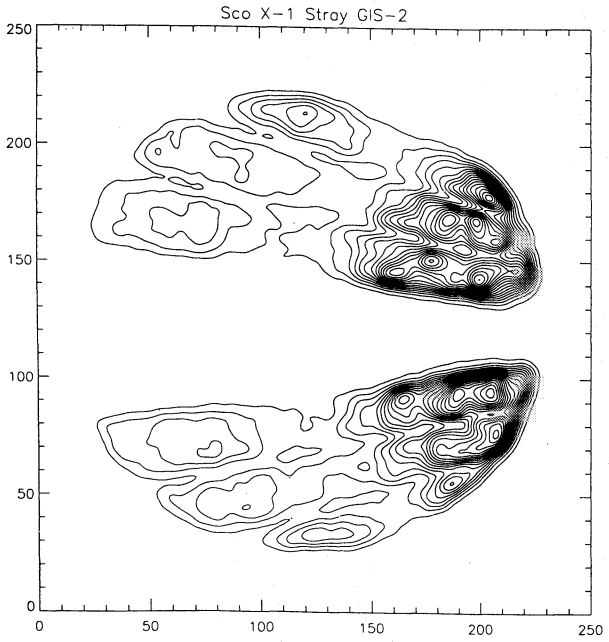

Fig. 11b. One degree off-axis observation of Sco X-1. The source is at 0° azimuth or to the right of the figure. This figure allows a direct comparison with the simulated result in figure 7b

to be 10% of the direct CXB flux at the detector center. The relative stray light contribution of course increases toward the edge of f.o.v. partly because of the decrease of efficiency of the direct CXB flux. At the same time, the stray light contamination is more serious for low energy X-rays, since substantial stray light is due to the back side reflection as mentioned above. The ratio of stray light to the direct CXB becomes 20% for 8 keV and 30% for 1.5 keV at a radius of 10′. At 20′, 30% and 55% for 8 and 1.5 keV, respectively.

5. Alignment

The relatively long XRT focal length, attained after extending the optical bench in a gravity free environment, following the usually severe launch conditions, are all factors that make it very difficult to accurately maintain alignment between each XRT and the corresponding detector, as well as co-alignment among the four telescopes. Measurements have indeed shown relative XRT displacements and tilting since the pre-launch alignments, manifested in two distinct ways. First, the four image centers have been displaced relative to each other, with the typical displacement being of order 1 mm. This effect may be explained by a rotation of the XRT mounting plate about the optical axis by as little as 10′. Telescope tilting does not affect the image centroid but changes the angular response and the effective area. To determine the post launch bore sights or maximum throughput directions we used two supernova remnants because of their fluxes, the Crab nebula and N132D in the Large Magellanic Cloud. These were observed at enough off-axis positions to allow us to infer the position of maximum transmission for each XRT. The four bore sights were found to scatter within about ±2′. This situation could arise from small amount of bending of the mounting plate following the optical bench extension. Both these types of offsets have been installed in the data analysis software.

6. Conclusions

Imaging spectroscopy over a broad energy band has become a reality with ASCA. For the first time, new exciting science is emerging from observations of various types of distant faint sources about which we knew very little before ASCA. The four XRT are performing almost precisely as designed and calibrated on the ground. At the same time, situations arise that make us keenly aware of two key limitations: The effective area at the upper end of the spectral band and the size of the image blur. As we begin to look at concepts of future spectroscopic instruments, we are confident that improvements in both these

important directions are forthcoming. The rich ASCA database will prove an extremely valuable guide toward our search for the best options for future spectrometers.

References

Aschenbach B. 1988, Appl. Opt. 27, 1404

Burke B.E., Mountain R.W., Harrison D.C., Bautz M.W., Doty J.P., Ricker G.R., Daniels P.J. 1991, IEEE Trans. ED-38, 1069

de Korte P.A.J., Giralt R., Coste J.N., Ernu C., Frindel S., Flamand J., Contet J.J. 1981, Appl. Opt. 20, 1080

Henke B.L., Lee P., Tanaka T.J., Shimabukuro R.L., Fujikawa B.K. 1982, Atomic Data and Nuclear Data Tables 27, 1

Kohmura Y., Fukazawa Y., Ikebe Y., Ishizaki Y., Kamijo S., Kaneda H., Makishima K., Matsushita K. et al. 1993, Proc. SPIE 2006, 78

Kohmura Y. et al. 1994, PASJ 46, L157

Kunieda H., Hayakawa S., Hirano T., Kii T. et al. 1986, Jpn. J. Appl. Phys. 25, 1292

Kunieda H., Tsusaka Y., Suzuki H., Ogasaka Y., Awaki H. et al. 1993, Jpn. J. Appl. Phys. 32, 4805

Ohashi T., Makishima K., Ishida M., Tsuru T., Tashiro M., Mihara T., Kohmura Y., Inoue H. 1991, Proc. SPIE 1549, 9

Ohashi T. et al. 1995, PASJ submitted

Serlemitsos P.J. 1981, NASA Tech. Mem. 83848, 441

Serlemitsos P.J. 1988, Appl. Opt. 27, 1447

Tanaka Y., Inoue H., Holt S.S. 1994, PASJ 46, L37

Tsusaka Y. et al. 1993, Proc. SPIE 2011, 517

Tsusaka Y. et al. 1995, Appl. Opt. submitted

Turner M. et al. 1989, PASJ 41, 345

Van Speybroeck L. 1979, Proc. SPIE 184, 2